ACCSCIENCE PUBLISHING

Materials Science in Additive Manufacturing

ORIGINAL RESEARCH ARTICLE

Welding-based algebraic models to predict microstructure features in laser powder bed fusion

Germán Omar Barrionuevo[1]*, Patricio Mendez[2], Jorge Ramos-Grez[3], and Iván La Fé-Perdomo[4]

[1]Department of Mechanical Engineering, Universidad San Francisco de Quito, Quito, Ecuador

[2]Department of Chemical and Materials Engineering, University of Alberta, Edmonton, Alberta, Canada

[3]Department of Mechanical and Metallurgical Engineering, School of Engineering, Pontifical Catholic University of Chile, Santiago, Chile

[4]Escuela de Ingeniería Mecánica, Pontificia Universidad Católica de Valparaíso, Quilpué, Chile

Abstract

Metal additive manufacturing has matured to the point where it is used ubiquitously in all types of industries, not only as a rapid prototyping technology, but also as a complement to and even a potentially superior manufacturing method compared to conventional processes. For industries that require high precision and process control, laser powder bed fusion (LPBF) is the preferred technology for processing advanced alloys. Researchers have developed complex models to predict material behavior during laser–material interaction with high accuracy. However, these models are difficult to implement and often require specific software. Therefore, this study evaluates the applicability of algebraic models used in welding to predict variables of interest in LPBF in a simple yet effective manner. The models used are based on the fundamental equations governing heat transfer in solids. The predicted quantities include melt-pool dimensions, sub-grain microstructure, and solidification time. The models show high accuracy in predicting microstructural features in the processing of 316L stainless steel manufactured using LPBF. The scanning speed is confirmed as a dominant control parameter governing both melt-pool geometry and microstructural features. Incorporating remelting and multi-layer effects improves analytical models beyond single-track assumptions, providing a more realistic representation of LPBF thermal behavior and capturing the cyclic nature of layer-by-layer construction.

Keywords: Laser powder bed fusion; Welding; Analytical modeling; Microstructure

***Corresponding author:**
Germán Omar Barrionuevo
(gbarrionuevo@usfq.edu.ec)

Citation: Barrionuevo GO, Mendez P, Ramos-Grez J, La Fé-Perdomo I. Welding-based algebraic models to predict microstructure features in laser powder bed fusion. *Mater Sci Add Manuf.* 2026;5(3):026050011. doi: 10.36922/MSAM026050011

Received: February 1, 2026

Revised: March 4, 2026

Accepted: March 6, 2026

Published online: May 18, 2026

1. Introduction

Laser powder bed fusion (LPBF) and fusion welding processes share a common physical basis, namely the interaction between a moving, highly concentrated heat source and a metallic substrate, followed by rapid melting and solidification under steep thermal gradients.[1–3] In both cases, the resulting thermal field governs melt-pool formation and solidification behavior, establishing a direct link between processing parameters and the final microstructure.

Classical welding heat-transfer models, particularly those derived from the Wilson–Rosenthal formulations[4,5], describe the temperature distribution induced by a traveling heat source in a semi-infinite solid and have long been employed to estimate cooling rates, solidification times, and characteristic microstructural length scales in welded joints. Despite the differences in spatial scale, energy density, and processing environment between welding and LPBF, the governing heat conduction mechanisms remain fundamentally comparable, providing a sound physical rationale for extending welding-based analytical models to additive manufacturing (AM) processes.[2,6,7]

Accurate prediction of thermal features in LPBF is crucial, as the temperature field generated by the moving laser directly controls melt-pool geometry, which in turn determines track continuity, interlayer bonding, and defect formation, including lack of fusion and keyholing.[8–10] Moreover, thermal gradients and cooling rates dictate microstructural evolution, phase stability, and grain morphology, thereby exerting a dominant influence on the mechanical performance and reliability of additively manufactured components.[11,12] Consequently, leveraging the extensive body of knowledge developed in fusion welding offers a promising pathway for understanding and controlling thermal phenomena in LPBF and establishing robust process–structure–property relationships.

From a physical perspective, melt-pool formation results from the balance between localized energy input, heat dissipation through conduction, and the relative motion of the heat source with respect to the material. When the supplied energy exceeds the melting enthalpy, a molten region forms, whose size and shape depend on process parameters and thermophysical properties.[13] Although the coupled thermal and fluid-flow phenomena involved are inherently complex, early analytical treatments demonstrated that valuable insight can be gained by approximating the process as a purely conductive heat-transfer problem under simplified assumptions.[10,14–16] The pivotal contribution in this regard is Wilson–Rosenthal's analytical solution for a moving point heat source in an infinite or semi-infinite medium, which provides a closed-form expression for the steady-state temperature field surrounding the heat source.

Originally developed for arc welding, this solution has since been widely adapted for laser welding, electron beam processing, and related high-energy-density thermal processes.[4,7,9] While Wilson–Rosenthal's solution yields the temperature distribution, it does not directly provide explicit expressions for melt-pool dimensions (i.e., length, width, and depth). These geometric parameters are typically obtained by imposing additional criteria on the temperature field, such as identifying the intersections of the melting isotherm with characteristic spatial directions or locating extrema of the temperature gradient.[14,17,18]

The resulting algebraic expressions for melt-pool dimensions offer several advantages. They enable rapid estimation of process outcomes without the computational expense of numerical simulations, reveal explicit scaling relationships between melt-pool geometry and key variables (e.g., heat input, scan speed, and thermal diffusivity), and serve as benchmark solutions for validating numerical heat-transfer models.[4,5,9,18,19] Despite these advantages, the limitations of analytical melt-pool models are well recognized. The assumption of purely conductive heat transfer neglects fluid flow within the molten pool driven by surface tension gradients, buoyancy forces, recoil pressure, and electromagnetic effects.[3,20]

Additionally, thermophysical properties are typically assumed constant, and latent heat, phase transformations, and evaporation losses are not explicitly considered. As a result, Wilson–Rosenthal-type models are most accurate under conduction-mode melting conditions and moderate energy inputs.[1,21] To mitigate these limitations, semi-analytical approaches, such as the Goldak double-ellipsoidal heat source model, have been developed, particularly for numerical simulations.[4,9,18,19] However, these models rely on fitted parameters and do not yield closed-form predictive expressions, which limits their transparency and generality.

In the context of metal AM, particularly LPBF, renewed interest has emerged in welding-based analytical models as tools for rapid assessment of thermal behavior. The small molten pools and extremely high cooling rates characteristic of LPBF make experimental quantification challenging, while full numerical simulations can be computationally intensive.[8,16,19,22,23] Within this framework, welding-derived algebraic expressions have demonstrated strong capability to predict key thermal parameters, including cooling rate and solidification time, especially for alloys such as LPBF-processed 316L stainless steel.[6] These parameters are directly linked to microstructural refinement, including cellular and dendritic sub-grain formation, and predicted values are generally consistent with finite element simulations and experimental observations when the models are applied within their validity domain.[2]

Classical Wilson–Rosenthal-type formulations and their Gaussian extensions (e.g., Eagar–Tsai) constitute the foundation of several works, achieving closed-form or semi-analytical expressions for melt-pool width and depth as functions of laser power, scanning speed, and thermophysical properties.[24,25] More recent studies have refined these approaches by incorporating process-dependent absorptivity, normalized enthalpy, or composite formulations that combine different analytical models to exploit their respective strengths (e.g., Gaussian-based width prediction with scaling-law–based depth estimation).[26–28] These developments have demonstrated that, within conduction-dominated regimes and for single-track conditions, analytical models can reproduce experimental melt-pool dimensions with reasonable accuracy while providing transparent physical insight, parameter sensitivity, and low computational cost, making them suitable for process mapping and first-order design in LPBF.

Overall, welding-based algebraic models represent a valuable and computationally efficient complement to numerical and experimental approaches in LPBF research. When employed with a clear understanding of their assumptions and limitations, they provide clear and transparent physical insight into the relationships between process parameters, thermal history, and microstructural evolution.[11,16,29,30]

In this context, the present work builds upon classical moving heat source theory to systematically analyze and apply analytical expressions for melt-pool dimensions under conduction-dominated conditions, extending the framework beyond a single layer by incorporating remelting effects, creating a model that can be extended to multiple-layer processes. In addition, details within the molten pool are analyzed, such as the size of the sub-grains and the cooling rate. By clarifying the origin, interpretation, and proper implementation of melt-pool width, length, and depth formulations, this study aims to resolve common ambiguities and reinforce the continued relevance of analytical modeling as a foundational tool in modern thermal processing and AM research.

2. Materials and methods

2.1. Sample preparation

Prismatic samples of austenitic stainless steel, grade AISI 316L, measuring 16 × 10 × 6 mm were fabricated using a GE-Colibrium equipment model Concept Laser MLAB 200R (Concept Laser GmbH, Germany); Figure 1), with a nominal chemical composition in wt% as follows: 16–18% chromium, 10–13% nickel, 2–2.5% molybdenum, ≤2% manganese, ≤1% silicon, ≤0.45% phosphorus, ≤0.3% carbon, ≤0.3% sulfur, and iron (as the balance). Based on a series of preliminary experiments[31,32], the optimized processing parameters were adopted as follows: laser power of 160 W with a laser beam diameter of around 80 µm, hatch spacing of 60 µm, and a layer thickness of 30 µm. A zig-zag scanning pattern was employed, rotating the scan direction by 67° in each subsequent layer. Furthermore, three scanning speeds were evaluated: 700, 900, and 1,100 mm/s to assess the model's capabilities. Nitrogen was used as the shielding gas to prevent oxidation.

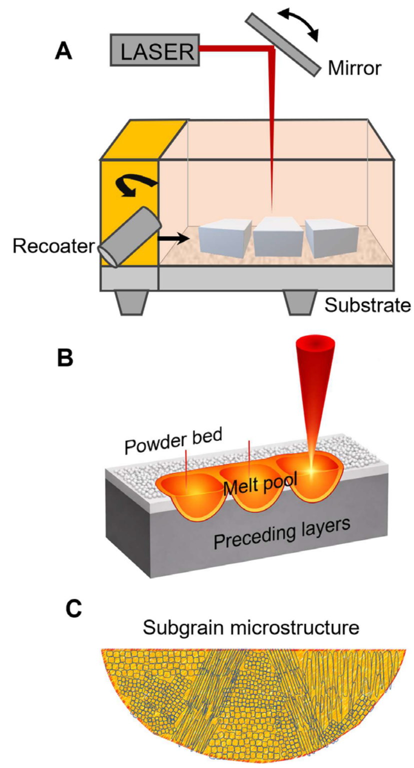

Figure 1. Microstructure evolution in laser powder bed fusion. (A) Schematic representation of the laser powder bed fusion (LPBF) process, (B) melt-pool formation during LPBF, and (C) sub-grain microstructure within molten pool.

2.2. Microstructure characterization

Additively manufactured samples were first ground using SiC paper for metallographic inspection, starting from 200 to 2,000 grits, and then finely polished using 0.1 µm diameter diamond paste. The microstructure was revealed by immersion etching in aqua regia (20 mL nitric acid and 60 mL hydrochloric acid) for approximately 10 s. Optical microscopy (MEIJI IM 7200, Meiji Techno Co., Japan) and scanning electron microscopy (SEM; TESCAN MIRA 3, TESCAN, Czech Republic) were employed for surface morphology analysis. Micrographs were processed and analyzed using Fiji software (v. 2.9.0, National Institutes of Health, USA) to determine microstructural features, namely melt-pool dimensions (Figure 1B) and sub-grain microstructure (Figure 1C).

For melt-pool quantification, measurements were performed on micrographs acquired from three different regions of the side surfaces. More than 30 molten pools were measured per condition. The results for the width, depth, and length are reported as both the average and the standard deviation.

2.3. Analytical modeling

The methodology employed was explicitly designed for engineering by reducing the heat-transfer problem to minimal representations governed by a small number of dimensionless groups, and by developing explicit predictive formulas for melt-pool dimensions.[4,5] Minimal representations are asymptotic idealizations of moving heat sources, which limit physical cases where secondary effects are negligible. In this case, a point heat source, a thick substrate, and a fast travel speed were considered.

The Wilson–Rosenthal equation (**Equation 1**) provides steady-state analytical temperature fields for a heat source moving at constant velocity (U) over a semi-infinite body. It is commonly used for estimating temperature contours and cooling rates away from the immediate melting zone, but it does not accurately predict the exact shape of the melt pool or temperatures near the source.

$$T_{(x,y,z)} = T_0 + \frac{q}{2\pi k r}\exp\left[-\frac{U}{2\alpha}(x+r)\right] \tag{1}$$

where q is the power absorbed ($P \times \eta$), P is the laser power, η corresponds to the process efficiency, U is the scanning speed, k is the thermal conductivity, α is the thermal diffusivity, r is the radial distance from the heat source, and x is the distance in the travel direction (Figure 2).

Other properties commonly used for analytical modeling include: c (specific heat capacity), i_{sl} (enthalpy of solidification), T_m (is the undercooling), and T_0 (room temperature). The thermophysical properties were determined through JMatPro software (v. 2.0, Sente Software Ltd., UK; Table 1). It is noteworthy that the rear melt-pool longitudinal coordinate corresponding to a certain isotherm value (e.g., melting temperature) is invariant with source speed for a given source power level.[5]

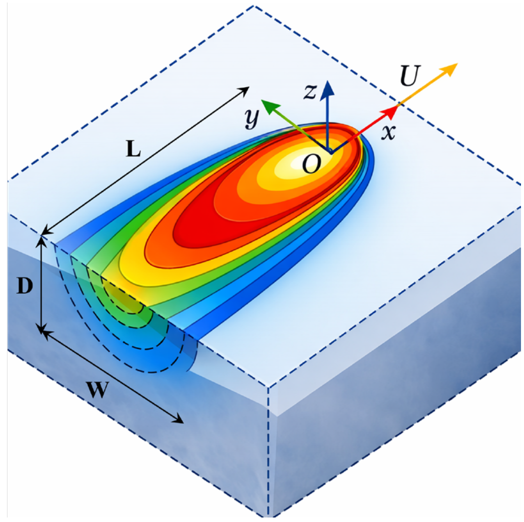

Figure 2. Schematic illustration of a point heat source in an infinite domain, highlighting the dimensions of the melt pool

Rykalin number (R_y), represented by **Equation 2**, is a crucial dimensionless parameter useful for modeling moving heat sources like those in welding and LPBF, representing the ratio of heat advection (movement) to conduction. A high R_y indicates a "fast" heat source where heat moves quickly (advection dominates), common in processes like laser welding.[1] In addition, dimensionless thickness (d^*) is calculated, capturing the physics of moving heat sources without requiring an arbitrary length scale (**Equation 3**). Both dimensionless metrics are used to construct regime maps, which partition parameter space into regions. Each regime represents a combination of parameters such that the system resembles a given minimal representation over others. Each regime corresponds to a dominant physical balance (e.g., fast/slow, two-dimensional/three-dimensional [3D], concentrated/distributed).[2]

$$R_y = \frac{qU}{4\pi k\alpha (T_m - T_0)} \tag{2}$$

$$d^* = \frac{Ud}{2\alpha} \tag{3}$$

Table 1. Thermophysical properties of the AISI 316L stainless steel

Thermal conductivity (k [W/m·K])	Specific heat capacity (c [J/kg·K])	Thermal diffusivity (α [m²/s])	Enthalpy of solidification (i_{sl} [J/kg])	Solidus temperature (T_s [K])	Liquidus temperature (T_l [K])
45.7	1.68×10^{-3}	3.4×10^{-6}	2.75×10^{5}	1,678	1,703

Once the processing conditions have been defined, equations inherent to each regime were applied. These algebraic models derived from exact analytical solutions provide a realistic approximation of the dimensions of the melt pool (Figure 2). For the algebraic solution, it is sufficient to know the thermal properties of the material; JMatPro software (v. 2.0, Sente Software Ltd., UK) was used to calculate the temperature variations up to the liquid state.

The melt-pool width is commonly estimated by imposing the melting isotherm on the Wilson–Rosenthal moving point-source solution and locating the maximum transverse extension, **Equations 4–6**. The factor *e* (Euler number) arises from evaluating the temperature field at the location of maximum transverse extent.

$$W = 2\sqrt{\frac{2\alpha q}{\pi e k U\left(T_m - T_0\right)}} \tag{4}$$

$$L = \frac{q}{2\pi e k\left(T_m - T_0\right)} \tag{5}$$

$$D = \sqrt{\frac{2\alpha q}{\pi e k U\left(T_m - T_0\right)}} \tag{6}$$

Based on preliminary experiments, modified analytical expressions incorporating semi-empirical corrections to account for remelting are proposed for modeling the geometrical characteristics of the molten pool in LPBF (**Equations 7–9**). The trailing edge of the molten pool is obtained from the logarithmic decay of the temperature field behind the heat source (**Equation 8**).

$$W \approx \sqrt{\frac{\pi e \alpha q}{kU\left(T_m - T_0\right)}} \tag{7}$$

$$L \approx \frac{4\alpha}{U}\ln\left(\frac{q}{2\pi e k\left(T_m - T_0\right)}\right) \tag{8}$$

$$D \approx \sqrt{\frac{e\alpha q}{\pi k U\left(T_m - T_0\right)}} \tag{9}$$

To obtain a more detailed evaluation of the thermal and microstructure features, the cellular cell spacing (λ_a), consistent with sub-grain size prediction, solidification time at the centerline (t_{sl}), and cooling rate (R) given by **Equations 10–12**, respectively, were calculated employing the processing parameters in LPBF; *A* and *n* are constants that were obtained from our previous research.[6] In this study, the values of *A* = 50 and *n* = 0.32 were used.

$$\lambda_a = A R^{-n} \tag{10}$$

$$t_{sl} = \frac{q\, i_{sl}\, \eta}{2\pi k c U\left(T_m - T_o\right)^2} \tag{11}$$

$$R = \frac{T_l - T_s}{t_{sl}} \tag{12}$$

3. Results

This section describes the experimental results of the microstructure of 316L stainless steel processed by LPBF and subsequently evaluates the predictions of the analytical models regarding the dimensions of the melt pool, as well as the size of the interdendritic arms characterized by cellular sub-grains within the melt pool.

3.1. Microstructure analysis

Figure 3 shows the characteristic microstructure of austenitic stainless steel processed using LPBF. On the side faces, the stacking of micro melt-pools can be observed, where their depth and width are influenced by the processing parameters, mainly the laser power and scanning speed.[31,33] On the upper surface, marks from the scanning strategy can be observed, as well as elliptical melt-pools corresponding to locally melted and rapidly solidified regions.

On the vertical faces, melt-pool boundaries are elongated and inclined, revealing the direction of heat flow from the molten pool into the underlying solidified layers. This finding highlights the strong thermal gradients oriented predominantly along the build direction, which drive epitaxial growth of grains across multiple layers.[29] Consequently, grains often span several layers, contributing to crystallographic texture and mechanical anisotropy. In contrast, the top surface shows a more planar and overlapping track pattern, directly associated with individual laser scan paths.[34] The difference between top and side views emphasizes that interpretations based on a single two-dimensional section may be misleading, as key features such as melt-pool depth and interlayer remelting are inherently three-dimensional.

Small dark regions visible within the volume correspond to microporosity or lack-of-fusion defects, which tend to align with melt-pool boundaries or track overlaps. Their spatial distribution can only be fully appreciated in a 3D reconstruction, reinforcing the importance of volumetric characterization for LPBF materials. A 3D perspective is essential for correctly relating processing parameters to the resulting microstructure and, ultimately, to mechanical and functional properties.

Figure 4 illustrates the characteristic melt-pool morphology of stainless steel processed by LPBF, emphasizing both in-plane and build-direction features.

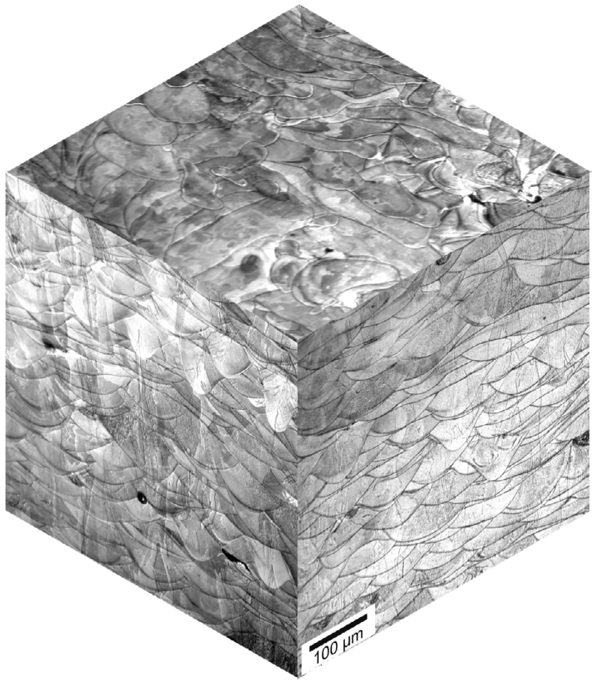

Figure 3. Three-dimensional assembly of optical micrographs of the stainless steel processed by laser powder bed fusion

Figure 4A shows that at the top surface, overlapping elliptical melt pools are aligned with the laser scan direction. Quantitative measurements at higher magnification (Figure 4B) show melt-pool widths and lengths on the order of approximately 100 to 200 μm, indicating a stable process regime with sufficient hatch overlap.

Figure 4C shows cross-sectional (side surface) micrographs highlighting the layer-wise stacking and partial remelting of melt pools, demonstrating strong metallurgical bonding between successive layers. Inside the melt pools, fine elongated and cellular sub-grains can be seen from the etched contrast (Figure 4D). This morphology is typical of LPBF stainless steels and results from extremely high cooling rates on the order of 10^5 to 10^6 K/s, which promote solute trapping and refined microstructures.[23] Measured melt-pool depths of around 50 μm exceed the nominal layer thickness, confirming interlayer remelting, which is essential for densification and microstructural continuity.[12]

Figure 5A shows a representative SEM micrograph in which successive melt pools overlap and stack as a result of the layer-by-layer LPBF process. The melt-pool boundaries correspond to individual laser tracks, and the remelted zones formed when a new layer partially remelts the underlying material. The orientation and intersection of these melt-pool boundaries reflect the laser scanning strategy (zig-zag) and the strong thermal gradients imposed during processing.[30] Within each melt pool, contrast variations indicate directional solidification, with fine solidification lines aligned approximately normal to the local melt-pool boundary. This is a hallmark of LPBF stainless steels and arises from epitaxial grain growth, where grains in the previously solidified layer act as substrates for subsequent solidification.[35,36] The stacking of melt pools evidences repeated thermal cycling, which is known to promote microstructural refinement but also contributes to anisotropy in mechanical behavior, particularly between the build direction and the scan plane.

Figure 5B provides a higher magnification view focused on the interior of a single melt pool, revealing a fine cellular or sub-grain network. The polygonal, equiaxed features are on the order of hundreds of nanometers and correspond to cellular sub-grains formed under extreme solidification conditions, mainly strong vertical thermal gradients, and high cooling rates.[37,38] These sub-grains are delineated by solute-enriched boundaries, often associated with elements such as chromium and molybdenum in stainless steels.[6]

The contrast between the upper and lower regions of the SEM micrographs reflects changes in the local thermal gradient and solidification velocity within the melt pool. Near the melt-pool boundary, cells tend to elongate along the heat flow direction, while more equiaxed cells form toward the interior.[11] This spatial variation illustrates how local thermal conditions within a single melt pool govern sub-grain morphology. Microstructural analysis showed that the cellular structures measured approximately 0.5 ± 0.1 μm.

While sub-grain (cellular) size in LPBF cannot be predicted exactly, it can be estimated using solidification theory, based on scaling laws that relate microstructural length scales to the local thermal conditions inside the melt pool.[30] In LPBF stainless steels, sub-grains are cellular solidification structures, not equilibrium grains.[35] Their size is controlled by the thermal gradient (G) at the solid–liquid interface and the cooling rate (R). Extremely high R (10^5–10^6 K/s) promotes cellular refinement and suppresses dendritic coarsening.

The sub-grain boundaries act as effective barriers to dislocation motion, contributing significantly to the enhanced yield strength and hardness typically reported for LPBF-processed stainless steels relative to their conventionally manufactured counterparts.[6] At the same time, the alignment of melt pools and grains explains the frequently observed mechanical anisotropy.[34]

It is worth noting that microstructural features, such as melt-pool dimensions and cellular sub-grain size, vary with processing parameters, particularly scanning speed

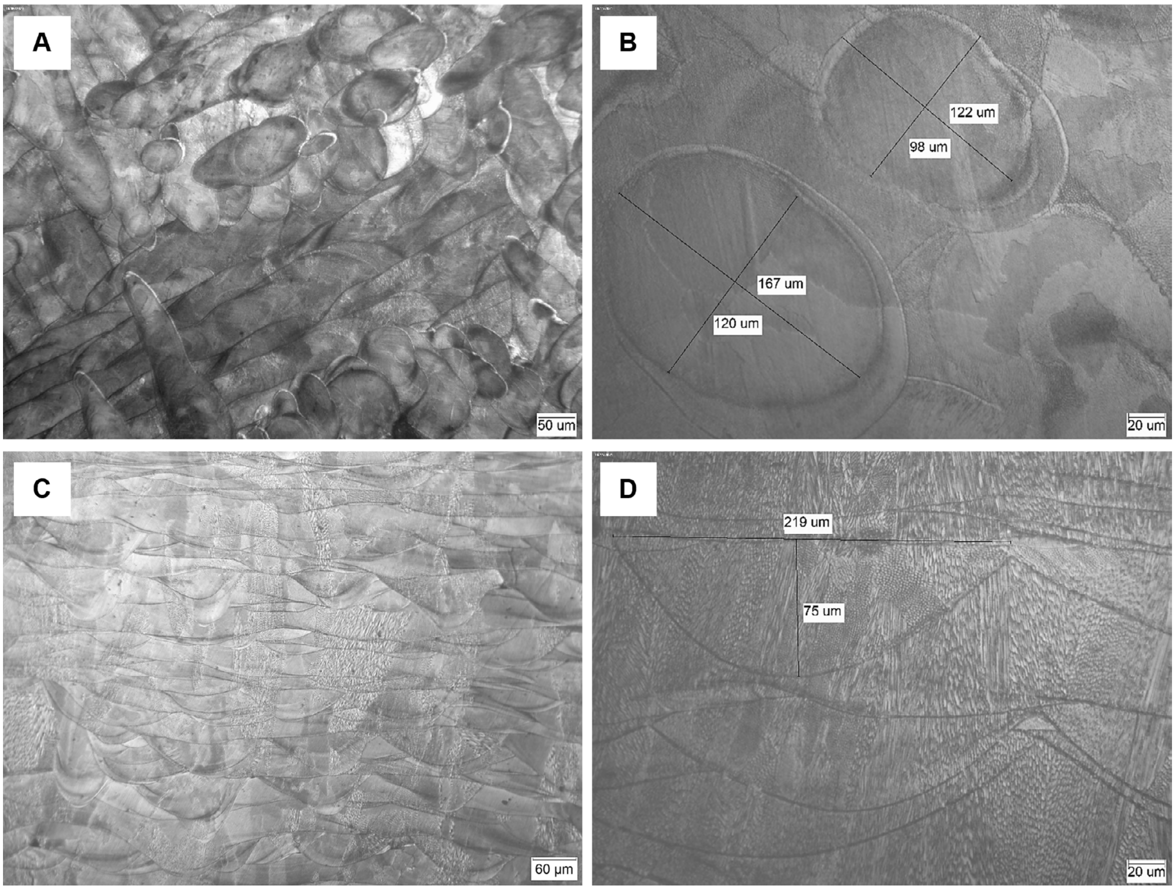

Figure 4. Representative optical micrographs of the stainless steel processed by laser powder bed fusion. (A) Top surface (magnification = 200×). (B) Elliptical melt pools at the top surface (magnification = 1,000×). (C) Side surface (magnification = 200×). (D) Melt-pool depth measurements at the side face (magnification = 1,000×).

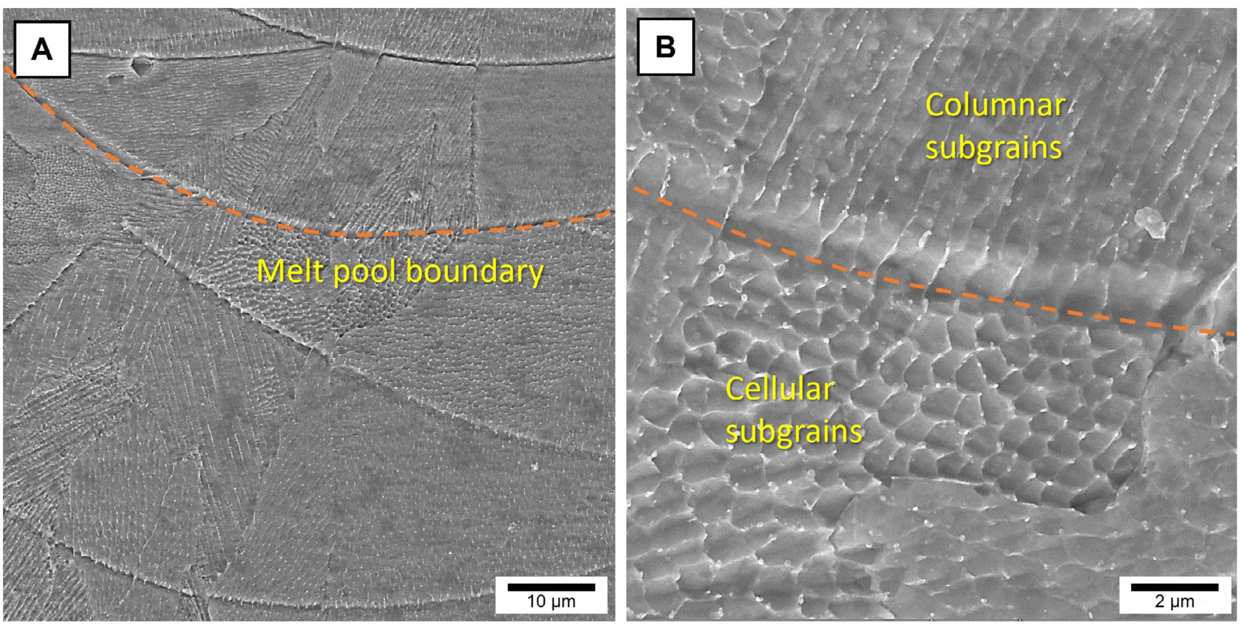

Figure 5. Scanning electron micrographs of the stainless steel processed by laser powder bed fusion. (A) Representative stacking of melt pools. (B) Cellular sub-grains within the melt pool.

Table 2. Experimental microstructural features as a function of the scanning speed

Scanning speed (U [mm/s])	Width (W [μm])	Depth (D [μm])	Length (L [μm])	Cell size (λ_a [μm])
700	178 ± 21	55 ± 14	201 ± 25	0.57
900	159 ± 22	49 ± 12	160 ± 34	0.53
1,100	146 ± 28	47 ± 18	128 ± 37	0.49

and laser power.[39] These microstructural features are summarized in Table 2.

3.2. Analytical modeling

Based on the methodology employed, considering a laser power of 160 W at a speed of 700 mm/s and a thickness (d) of 6 mm, values of R_y = 13.13 and a d^* = 617.6 were obtained. Therefore, the process falls within Regime I, corresponding to a fast heat source on a thick substrate.[2] Table 3 shows the results obtained by varying the scanning speed; as the Rykalin number has a linear relationship with the scanning speed, it was analyzed whether variations in speed affect the regime and, consequently, the equations that govern the system behavior. On the other hand, if the thickness of the sample is reduced, tending toward a few melt pools (<100 μm), the regime tends to approach the origin; that is, it approaches shared regimes, where it is necessary to use correction factors.[40] Once it has been verified that the system operates in Regime I, the geometry of the melt pool is calculated, as well as its microstructural features.

Figure 6 shows the predicted melt-pool dimensions and compares them with the results obtained experimentally. Notably, due to the high geometric variability within the melt pool, the experimental results show significant dispersion with respect to the length and depth of the melt pool.

On the one hand, the proposed analytical model is accurate in determining the depth and width of the melt pool, with a relative error of less than 5% for all the evaluated cases. On the other hand, the results for the melt-pool length show a higher percentage error (<10%). These results may be associated with measurement errors, since, as shown in Figure 4A, the geometric variability of the melt pool on the upper face is significant.

From Figure 6, it is also possible to extrapolate the effect of scanning speed on the variation in the dimensions of the melt pool. In all cases, it can be seen that lower speeds result in larger dimensions (i.e., the melt pool grows). This occurs because the laser beam has more time to completely melt the metal powder.[41] According to previous studies, scanning speed is a significant parameter that, in addition to affecting the dimensions of the melt pool, also influences properties such as relative density and surface roughness.[31]

Analytical melt-pool dimensions can be estimated by imposing the melting isotherm on Wilson–Rosenthal-type moving heat source solutions, yielding closed-form expressions for melt-pool width, depth, and length. Such models neglect convective transport and keyhole effects; nonetheless, they remain useful for rapid process window estimation and model validation.[42,43]

Figure 7 shows the results of the effect of scanning speed on cellular sub-grain spacing. According to the selected processing parameters, the cell size ranges between 500

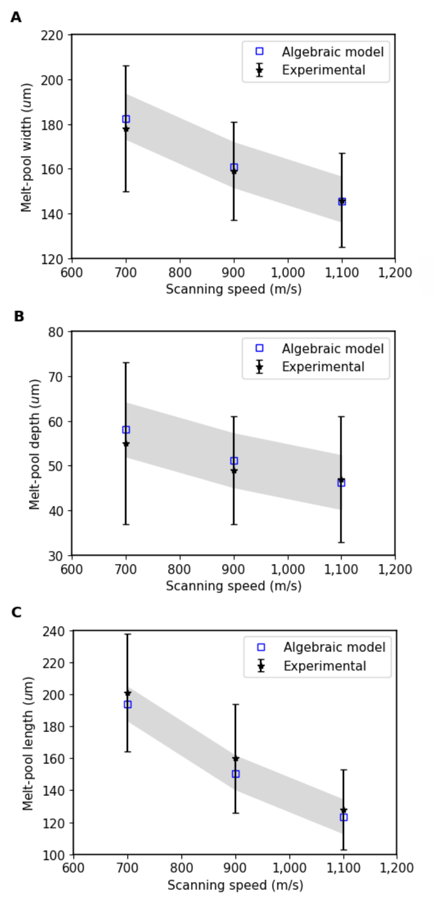

Figure 6. Comparative evaluation of the experimental and analytical melt-pool dimensions: (A) width, (B) depth, and (C) length

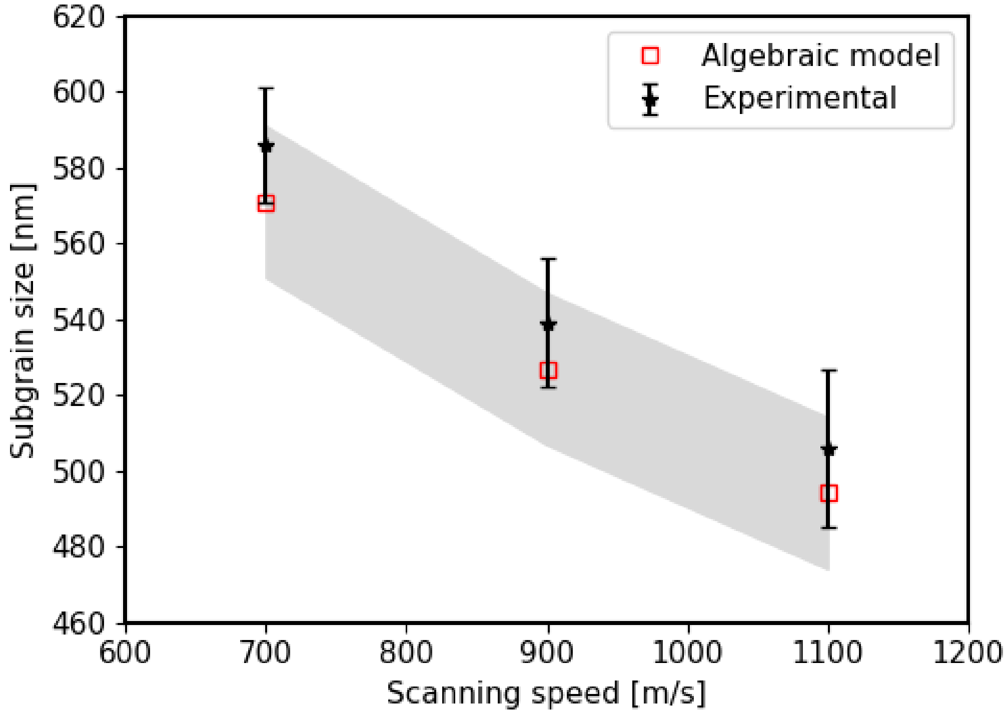

Figure 7. Comparative evaluation of the experimental and analytical cellular sub-grain size

Table 3. Regimes as a function of the scanning speed

Scanning speed (U [mm/s])	Rykalin number (R_y)	Dimensionless thickness (d^*)	Regime
700	13.13	617.6	I
900	16.88	794.1	I
1,100	20.64	970.6	I

and 600 nm. Additionally, the same pattern detected in the dimensions of the melt pool could be observed; that is, there is an inverse relationship between the size of the cellular sub-grains and the scanning speed. At higher scanning speeds, the laser has less contact time to interact with the substrate and, consequently, a higher cooling rate (R) is achieved.

As shown in Figure 7, the cellular sub-grain size can be accurately predicted using an algebraic expression that has been widely used in welding studies. One of the main differences in AM is the extremely high cooling rate, on the order of 10^5 to 10^6 K/s in LPBF.[44,45] The predicted sub-grain sizes fall in the sub-micrometer range, which is in good agreement with SEM observations (Figure 5B), where values around 600 nm were obtained.

4. Discussion

The algebraic expressions are derived from exact analytical solutions of the Wilson–Rosenthal equation by applying normalization, dimensional analysis, asymptotic analysis, and blending techniques related to an isotherm that can be expressed as a dimensionless expression dependent only on the Rykalin number (R_y).[1,2,40]

For the evaluated processing parameter window, the calculated Rykalin number (R_y = 13–21) places the process in Regime I (fast heat source, thick substrate), where conduction dominates over advective transport. Experimentally measured melt-pool aspect ratios (D/W < 0.4) and depths (approximately 50 µm) are consistent with conduction-mode melting and remain far below typical keyhole penetration (>100–150 µm for this power level). No keyhole porosity or deep vapor cavities were observed (Figures 4 and 5), further supporting this assumption.

It is worth noting that the model begins to fail when the energy density increases to the point where: (i) the depth-to-width ratio increases sharply, (ii) vapor recoil pressure induces cavity formation, and (iii) the melt-pool morphology transitions from elliptical to a narrow and deep geometry characteristic of keyhole mode.

Figure 8 shows the main features of the melt pool that were determined in this study. These range from the overall dimensions of the pool to detailed characteristics within it. Despite these achievements, predictive capability deteriorates in transitional and keyhole regimes, particularly at high energy densities, and for complex geometries or scan strategies, often requiring empirical calibration to maintain accuracy.[8,12,38,41,46]

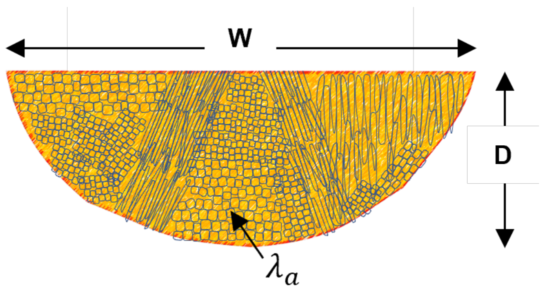

Figure 8. Main features of the melt pool determined in this study
Abbreviations: D: Depth; W: Width.

Even extended or composite analytical models, while improving agreement for specific metrics or materials, remain case-dependent and cannot fully capture the strongly coupled, multiphysics nature of LPBF melt-pool dynamics.[42,43,46] Therefore, analytical models are best regarded as physically informed, first-order predictive tools whose validity is confined to well-defined processing windows, rather than comprehensive substitutes for high-fidelity numerical or experimental approaches.[47]

Table 4 presents a range of values for the melt-pool dimensions and sub-grain size reported in the literature for the main alloys used in LPBF. On the one hand, the values obtained in this study fall within the ranges commonly observed in the processing of 316L stainless steel.[33] On the other hand, the relatively narrow range of values obtained results from the fact that the processing parameters were optimized to achieve a maximum relative density.[31]

Although this study is only valid for austenitic stainless steel alloys, it may be extrapolated to other materials, where, before using **Equations 7–9**, calibration must be performed through experimental testing.

Despite their simplifying assumptions, algebraic models retain strong predictive value as first-order engineering tools for LPBF process design. Most models previously developed consider only single-track problems.[16,52] In this study, the geometry of several stacked melt pools was analyzed, considering remelting, and consequently, a more realistic representation of the LPBF process was obtained. When applied with clear awareness of their assumptions and regime limitations, welding-based algebraic models offer unique physical insight into process–structure relationships and help guide more resource-intensive numerical and experimental studies.

Table 4. Reported ranges of microstructure features for the main alloys used in laser powder bed fusion

Alloy	Width (μm)	Depth (μm)	Length (μm)	λ_a (μm)	Reference
316L	145–180	45–55	130–205	0.49–0.57	The present study
AlSi10Mg	80–160	30–80	150–350	0.3–0.8	48
Inconel 718	120–250	40–100	200–400	0.5–1.5	49
Ti-6Al-4V	100–220	30–90	180–350	0.8–2.0	50
18Ni-300 maraging steel	120–240	40–100	220–380	0.4–1.2	51

5. Conclusion

This study evaluated the use of algebraic models commonly used in welding to calculate melt-pool dimensions and sub-grain sizes in stainless steel processed by LPBF. The main findings are detailed below:

(i) Melt-pool width and depth in LPBF-processed 316L stainless steel can be predicted with high accuracy using closed-form algebraic expressions. The proposed analytical formulations yielded relative errors below 5% for melt-pool width and depth across all evaluated scanning speeds, confirming that conduction-based models are reliable for estimating the primary geometric features of the melt pool in stable LPBF processing windows.
(ii) Scanning speed is confirmed as a dominant control parameter governing both melt-pool geometry and microstructural refinement. Increasing scanning speed systematically reduces melt-pool dimensions and increases cooling rates, leading to

finer cellular sub-grain spacing. This analytical–experimental consistency reinforces the direct linkage between process parameters, thermal history, and microstructure in LPBF.

(iii) Cellular sub-grain size in LPBF 316L stainless steel can be accurately estimated using solidification-based scaling laws originally developed for welding. The predicted sub-grain spacings range from approximately 500 to 600 nm, closely matching SEM observations, demonstrating that algebraic cooling-rate–based models remain valid even under the extreme solidification conditions characteristic of LPBF (10^5–10^6 K/s).

(iv) The integration of remelting and multi-layer effects represents a significant advancement over conventional single-track analytical models. By accounting for stacked melt pools and interlayer remelting, the study offers a more realistic representation of LPBF thermal behavior, bridging the gap between idealized analytical solutions and the inherently cyclic nature of AM.

Acknowledgements

The authors gratefully acknowledge the support of the Canadian Centre for Welding and Joining.

Funding

This research was financially supported by the Universidad San Francisco de Quito USFQ, through the POLIGRANT project ID 41977.

Conflict of interest

Germán Omar Barrionuevo serves as an Editorial Board Member of the journal, but did not in any way participate in the editorial and peer-review process conducted for this paper, directly or indirectly. Other authors declare they have no competing interests.

Author contributions

Conceptualization: Patricio Mendez
Investigation: Germán Omar Barrionuevo, Jorge Ramos-Grez, Iván La Fé-Perdomo
Methodology: Patricio Mendez, Germán Omar Barrionuevo
Writing–original draft: Germán Omar Barrionuevo
Writing–review and editing: Patricio Mendez, Jorge Ramos-Grez, Iván La Fé-Perdomo

Ethics approval and consent to participate

Not applicable.

Consent for publication

Not applicable.

Availability of data

Data are available from the corresponding author on reasonable request.

References

1. Wang Y, Lu Y, Mendez PF. Scaling expressions of characteristic values for a moving point heat source in steady state on a semi-infinite solid. *Int J Heat Mass Transf*. 2019;135:1118-1129.

   doi: 10.1016/j.ijheatmasstransfer.2019.02.042

2. Mendez PF. Calculation of thermal features in welding and additive manufacturing. *IOP Conf Ser Mater Sci Eng*. 2023;1281(1):012021.

   doi: 10.1088/1757-899X/1281/1/012021

3. Nabavi SF, Farshidianfar A, Dalir H. A comprehensive review on recent laser beam welding process: geometrical, metallurgical, and mechanical characteristic modeling. *Int J Adv Manuf Technol*. 2023;129(11-12):4781-4828.

   doi: 10.1007/s00170-023-12536-1

4. Keeley W, Turner R, Mitchell B, Warnken N. A Development of the Rosenthal Equation for Predicting Thermal Profiles During Additive Manufacturing. *Thermo*. 2025;5(2):16.

   doi: 10.3390/thermo5020016

5. Ramos-Grez JA, Sen M. Analytical, quasi-stationary Wilson-Rosenthal solution for moving heat sources. *Int J Therm Sci*. 2019;140:455-465.

   doi: 10.1016/j.ijthermalsci.2019.03.017

6. Barrionuevo GO, La Fé-Perdomo I, Ramos-Grez JA, Walczak M, Mendez PF. Microstructural differences and mechanical performance of stainless steel 316L conventionally processed versus a selective laser melted. *Prog Addit Manuf*. 2025;10(4):2663-2673.

   doi: 10.1007/s40964-024-00774-y

7. Soundararajan B, Sofia D, Barletta D, Poletto M. Review on modeling techniques for powder bed fusion processes based on physical principles. *Addit Manuf*. 2021;47:102336.

   doi: 10.1016/j.addma.2021.102336

8. Liu J, Wu X, Wang D, *et al*. Multi-physics modeling of laser melted magnesium alloy: Bridging melt pool dynamics to microstructure evolution. *J Magnes Alloys*. 2025;13(12):6167-6182.

   doi: 10.1016/j.jma.2025.06.032

9. Jiménez-Xamán M, Hernández-Hernández M, Tariq R, *et al*. Numerical simulations and mathematical models in laser welding: a review based on physics and heat source models. *Front Mech Eng*. 2024;10:1325623.

   doi: 10.3389/fmech.2024.1325623

10. Solyaev Y, Lurie S. Gradient models of moving heat sources

for powder bed fusion applications. *Int J Heat Mass Transf*. 2022;196:123221.

doi: 10.1016/j.ijheatmasstransfer.2022.123221

11. Sinha S, Mukherjee T. Effects of beam shaping on temperature, pool geometry, and cooling rate in laser powder bed fusion. *Manuf Lett*. 2025;45:53-59.

    doi: 10.1016/j.mfglet.2025.06.210

12. Schlenger L, Nasab MH, Masinelli G, *et al*. Fast and accurate laser powder bed fusion metamodels predicting melt pool dimensions, effective laser absorptivity and lack of fusion defects. *J Manuf Process*. 2025;141:1337-1353.

    doi: 10.1016/j.jmapro.2025.03.006

13. Lu H, Pan J, Gu Y, *et al*. Comparison of melt evolution and flow mechanisms of Inconel 718, Ti6Al4V, 304 stainless steel, and AlSi10Mg manufactured by laser powder bed fusion, structures, and properties after heat treatments. *Mater Sci Eng A*. 2023;865:144649.

    doi: 10.1016/j.msea.2023.144649

14. Lu Y, Wang Y, Mendez PF. Width of thermal features induced by a 2-D moving heat source. *Int J Heat Mass Transf*. 2020;156:119793.

    doi: 10.1016/j.ijheatmasstransfer.2020.119793

15. Gupta SK, Patil AP, Rathod RC, Tandon V, Vashishtha H. Investigation on Impact of Heat Input on Microstructural, Mechanical, and Intergranular Corrosion Properties of Gas Tungsten Arc-Welded Ti-Stabilized 439 Ferritic Stainless Steel. *J Mater Eng Perform*. 2022;31(5):4084-4097.

    doi: 10.1007/s11665-021-06512-7

16. Zhang ZD, Imani Shahabad S, Ibhadode O, Dibia CF, Bonakdar A, Toyserkani E. 3-Dimensional heat transfer modeling for laser powder bed fusion additive manufacturing using parallel computing and adaptive mesh. *Opt Laser Technol*. 2023;158:108839.

    doi: 10.1016/j.optlastec.2022.108839

17. Azar AS, Ås SK, Akselsen OM. Determination of welding heat source parameters from actual bead shape. *Comput Mater Sci*. 2012;54:176-182.

    doi: 10.1016/j.commatsci.2011.10.025

18. Yadav A, Ghosh A, Kumar A. Experimental and numerical study of thermal field and weld bead characteristics in submerged arc welded plate. *J Mater Process Technol*. 2017;248:262-274.

    doi: 10.1016/j.jmatprotec.2017.05.021

19. Khan A, Jaffery SHI, Hussain SZ, Anwar Z, Dilawar S. Numerical and Experimental Characterization of Melt Pool in Laser Powder Bed Fusion of SS316l. *Integrating Mater Manuf Innov*. 2023;12(3):210-230.

    doi: 10.1007/s40192-023-00302-w

20. Ko T, Kim H, Shin Y, *et al*. Review of Recent Additive Manufacturing and Welding Research with Application of Physics-Informed Neural Networks. *J Weld Join*. 2024;42(4):357-365.

    doi: 10.5781/JWJ.2024.42.4.3

21. Prisco U. Shape of the melt pool produced by a moving Gaussian heat source. *Weld World*. 2021;65(11):2105-2118.

    doi: 10.1007/s40194-021-01167-3

22. Irwin JE, Wang Q, Michaleris P (Pan), Nassar AR, Ren Y, Stutzman CB. Iterative simulation-based techniques for control of laser powder bed fusion additive manufacturing. *Addit Manuf*. 2021;46:102078.

    doi: 10.1016/j.addma.2021.102078

23. Barrionuevo GO, Calvopiña H, Debut A, Pérez-Salinas C. Experimental and numerical investigation of sliding wear of heat-treated 316L stainless steel additively manufactured. *J Mater Res Technol*. 2024;33:2692-2703.

    doi: 10.1016/j.jmrt.2024.09.263

24. Coen V, Goossens L, Hooreweder BV. Methodology and experimental validation of analytical melt pool models for laser powder bed fusion. *J Mater Process Technol*. 2022;304:117547.

    doi: 10.1016/j.jmatprotec.2022.117547

25. Wang W, Ning J, Garmestani H, Liang SY. Analytical Prediction of Molten Pool Dimensions in Powder Bed Fusion Considering Process Conditions-Dependent Laser Absorptivity. *Appl Sci*. 2022;12(23):11926.

    doi: 10.3390/app122311926

26. Zagade PR, Gautham BP, De A, DebRoy T. Analytical modelling of scanning strategy effect on temperature field and melt track dimensions in laser powder bed fusion. *Addit Manuf*. 2024;82:104046.

    doi: 10.1016/j.addma.2024.104046

27. Rangaswamy S, Bourke D, Monu MCC, *et al*. Investigating Melt Pool Dimensions in Laser Powder Bed Fusion of Nitinol: An Analytical Approach. *Adv Eng Mater*. 2024;26(24):2401636.

    doi: 10.1002/adem.202401636

28. Correa-Gómez E, Moock VM, Caballero-Ruiz A, Ruiz-Huerta L. Improving melt pool depth estimation in laser powder bed fusion with metallic alloys using the thermal dose concept. *Int J Adv Manuf Technol*. 2024;135(7-8):3463-3471.

    doi: 10.1007/s00170-024-14700-7

29. Kang K, Yuan L, Phillion AB. A 3D simulation of grain structure evolution during powder bed fusion additive manufacturing and subsequent laser rescanning process. *J Mater Process Technol*. 2024;333:118603.

    doi: 10.1016/j.jmatprotec.2024.118603

30. Özel EF, Pede D, Müller C, Thomann Y, Thomann R, Mozaffari-Jovein H. Microstructure of Selective Laser Melted 316L under Non-Equilibrium Solidification Conditions. *J Exp Theor Anal*. 2023;1(2):64-73.

doi: 10.3390/jeta1020005

31. Barrionuevo GO, Ramos-Grez JA, Sánchez-Sánchez X, Zapata-Hidalgo D, Mullo JL, Puma-Araujo SD. Influence of the Processing Parameters on the Microstructure and Mechanical Properties of 316L Stainless Steel Fabricated by Laser Powder Bed Fusion. *J Manuf Mater Process*. 2024;8(1):35.

doi: 10.3390/jmmp8010035

32. La Fé-Perdomo I, Loyola O, Barrionuevo GO, Ramos-Grez JA. Adiabatic efficiency and mechanical properties optimization for the laser-based powder bed fusion process of 316L stainless steel alloy. *Mater Today Commun*. 2025;49:113616.

doi: 10.1016/j.mtcomm.2025.113616

33. Liverani E, Toschi S, Ceschini L, Fortunato A. Effect of selective laser melting (SLM) process parameters on microstructure and mechanical properties of 316L austenitic stainless steel. *J Mater Process Technol*. 2017;249:255-263.

doi: 10.1016/j.jmatprotec.2017.05.042

34. Barrionuevo GO, Ramos-Grez JA, Walczak M, *et al*. Microstructure simulation and experimental evaluation of the anisotropy of 316 L stainless steel manufactured by laser powder bed fusion. *Rapid Prototyp J*. 2023;29(3):425-436.

doi: 10.1108/RPJ-04-2022-0127

35. Li Y, Jiang P, Li Y, Mi G, Geng S. Microstructure evolution and mechanical properties in the depth direction of ultra-high power laser-arc hybrid weld joint of 316L stainless steel. *Opt Laser Technol*. 2023;160:109093.

doi: 10.1016/j.optlastec.2022.109093

36. Li F, Liu Y, Kong H, Sun Q, Kang K, Sun Q. Improved microstructure and performance of thick-walled 316L stainless steel joint by NG-GTAW with auxiliary magnetic field. *J Mater Res Technol*. 2022;21:3038-3050.

doi: 10.1016/j.jmrt.2022.10.109

37. Wu Z, Narra SP, Rollett A. Exploring the fabrication limits of thin-wall structures in a laser powder bed fusion process. *Int J Adv Manuf Technol*. 2020;110(1-2):191-207.

doi: 10.1007/s00170-020-05827-4

38. Manav M, Perraudin N, Lin Y, *et al*. MeltpoolINR: predicting temperature field, melt pool geometry and their rate of change in laser powder bed fusion. *J Intell Manuf*. Published online October 18, 2025.

doi: 10.1007/s10845-025-02692-4

39. Alaparthi S, Subadra SP, Skaria R, Mayer E, Sheikhi S. A study on the effect of print parameters on the internal structural quality of 316 L samples printed via laser powder bed fusion: Experimental and algorithmic approach. *Eng Rep*. 2024;6(12):e12996.

doi: 10.1002/eng2.12996

40. Wang Y, Mendez PF. Isotherm penetration depth under a moving Gaussian surface heat source on a thick substrate. *Int J Therm Sci*. 2022;172:107334.

doi: 10.1016/j.ijthermalsci.2021.107334

41. Kumar PD, Kavitha S, Khan MA, Jappes JTW. Linking computational models with experimental evidence for mechanical analysis of additive built stainless steel material. *Prog Addit Manuf*. Published online February 11, 2026.

doi: 10.1007/s40964-025-01513-7

42. Zhang T, Lin X, Qin Y, *et al*. Multiphysics Modeling of Heat Transfer and Melt Pool Thermo-Fluid Dynamics in Laser-Based Powder Bed Fusion of Metals. *Materials*. 2025;18(13):3183.

doi: 10.3390/ma18133183

43. Queva A, Guillemot G, Moriconi C, Bergeron R, Bellet M. Mesoscale multilayer multitrack modeling of melt pool physics in laser powder bed fusion of lattice metal features. *Addit Manuf*. 2024;93:104365.

doi: 10.1016/j.addma.2024.104365

44. Kosiba K, Gustmann T, Kim JT, *et al*. Experimental cooling rates during high-power laser powder bed fusion at varying processing conditions. *J Alloys Compd*. 2023;967:171773.

doi: 10.1016/j.jallcom.2023.171773

45. Thampy V, Fong AY, Calta NP, *et al*. Subsurface Cooling Rates and Microstructural Response during Laser Based Metal Additive Manufacturing. *Sci Rep*. 2020;10(1):1981.

doi: 10.1038/s41598-020-58598-z

46. Shi L, Xu S, Hou Y, *et al*. Multi-Scale Numerical Modeling and Experimental Study of Molten Pool Dynamics and Solidification During the Additive Manufacturing of Inconel 718 Superalloy. *Metall Mater Trans B*. 2025;56(5):5773-5790.

doi: 10.1007/s11663-025-03732-3

47. Lin X, Mao Y, Wu L, Zhu K. Melt pool super solution reconstruction based on dual path deep learning for laser powder bed fusion monitoring. *Mater Sci Addit Manuf*. 2024;3(4):5585.

doi: 10.36922/msam.5585

48. Mishra AK, Kumar A. Effect of Process Parameters on Melt Pool Characteristics and Solidification Process During Laser Powder Bed Fusion of AlSi10Mg Alloy. *Lasers Manuf Mater Process*. 2024;11(2):260-283.

doi: 10.1007/s40516-023-00243-4

49. Li L, Chen H, Wang X, Liao Z. Effects of vector length on the melt pool morphology and grain structure characteristics

of Alloy 718 in laser powder bed fusion. *J Mater Process Technol*. 2024;326:118317.

doi: 10.1016/j.jmatprotec.2024.118317

50. Cao Z, Liu Y, Shen J, *et al*. Effect of melt pool interference modes on mesostructure and microstructure of laser powder bed fusion fabricated Ti-6Al-4V alloy. *Mater Sci Eng A*. 2026;958:149944.

doi: 10.1016/j.msea.2026.149944

51. Song J, Song B, Ryan M, Setchi R, Shi Y. Thermal behaviour and fluid dynamics during pulsed-wave laser powder bed fusion of 18Ni-300 maraging steel. *J Mater Sci Technol*. 2026;249:287-304.

doi: 10.1016/j.jmst.2025.05.063

52. Guo K, Qiao L, Huang Z, Anwer N, Cao Y. A computational model of melt pool morphology for selective laser melting process. *Int J Adv Manuf Technol*. 2022;121(3-4):1651-1673.

doi: 10.1007/s00170-022-09366-y